

Deglacial Subantarctic CO₂ outgassing driven by a weakened solubility pump

Received: 9 July 2022

Yuhao Dai ^{1,4}✉, Jimin Yu ^{2,1}✉, Haojia Ren ³ & Xuan Ji¹

Accepted: 23 August 2022

Published online: 03 September 2022

 Check for updates

The Subantarctic Southern Ocean has long been thought to be an important contributor to increases in atmospheric carbon dioxide partial pressure (pCO₂) during glacial-interglacial transitions. Extensive studies suggest that a weakened biological pump, a process associated with nutrient utilization efficiency, drove up surface-water pCO₂ in this region during deglaciations. By contrast, regional influences of the solubility pump, a process mainly linked to temperature variations, have been largely overlooked. Here, we evaluate relative roles of the biological and solubility pumps in determining surface-water pCO₂ variabilities in the Subantarctic Southern Ocean during the last deglaciation, based on paired reconstructions of surface-water pCO₂, temperature, and nutrient utilization efficiency. We show that compared to the biological pump, the solubility pump imposed a strong impact on deglacial Subantarctic surface-water pCO₂ variabilities. Our findings therefore reveal a previously underappreciated role of the solubility pump in modulating deglacial Subantarctic CO₂ release and possibly past atmospheric pCO₂ fluctuations.

The Southern Ocean is widely regarded as a crucial source of carbon dioxide (CO₂) to the atmosphere during glacial terminations because this region serves as a window for CO₂ exchanges between the atmosphere and the ocean interior^{1–4}. In the Southern Ocean, prevailing southern hemisphere westerly winds drive upwelling of carbon-rich deep waters surrounding Antarctica, some of which are transported northward to the Subantarctic Zone (SAZ)^{5,6}. The surface SAZ exposes the newly upwelled carbon-rich deep waters to the atmosphere enabling CO₂ outgassing, before these waters are entrained to form intermediate and mode waters^{5–7}.

Changes in the SAZ have been thought to be critical to deglacial atmospheric pCO₂ rises, with a contribution estimated to be around 40 ppm^{8–11}. In the SAZ, CO₂ tends to escape to the atmosphere due to elevated surface-water CO₂ partial pressures (pCO₂) driven by high surface-water dissolved inorganic carbon (DIC) concentrations^{12,13} associated with the newly upwelled deep waters surrounding Antarctica. CO₂ outgassing in the SAZ is somewhat alleviated by biologically driven carbon sequestration that exports carbon to depths in the form

of organic matter, a process called the biological pump^{1,14,15}. In addition to this biological process, it is important to note that surface-water pCO₂ is further affected by CO₂ solubility determined by seawater temperature and salinity, a process known as the solubility pump^{14,16}. Changes in the solubility pump have been shown by modeling studies to contribute substantially to atmospheric pCO₂ variability^{2,17–19}. Everything else being equal, warming lowers CO₂ solubility in seawater and thus increases surface-water pCO₂ with an effect to cause CO₂ outgassing from the ocean to the atmosphere¹⁶. Surface-water pCO₂ increases with increasing salinity, but the salinity effect on the CO₂ solubility is generally smaller than the temperature effect in most regions²⁰ (Supplementary Fig. 2).

During glacial terminations, it has been proposed that the biological pump efficiency was lowered, driving up CO₂ outgassing in the SAZ^{1,11,21–23}. The deglacial SAZ biological pump efficiency decline has been linked to reduced supplies of micronutrients such as iron via eolian lithogenic fluxes^{10,11,24}. In this case, weakened biological pump would leave more carbon unused in the SAZ surface, raising

¹Research School of Earth Sciences, The Australian National University, Canberra, ACT, Australia. ²Pilot National Laboratory for Marine Science and Technology (Qingdao), Qingdao, China. ³Department of Geosciences, National Taiwan University, Taipei, Taiwan. ⁴Present address: Department of Geology, Lund University, Lund, Sweden. ✉e-mail: yuhao.dai@geol.lu.se; jiminyuanu@gmail.com

surface-water $p\text{CO}_2$ which would stimulate CO_2 outgassing¹. On the other hand, as manifested by Southern Ocean temperature reconstructions^{25–27}, deglacial SAZ warming, in theory, should weaken the solubility pump, raise surface-water $p\text{CO}_2$, and promote CO_2 outgassing¹⁶ (Supplementary Fig. 1). Existing reconstructions in the SAZ indeed show elevated surface-water $p\text{CO}_2$ during the last deglaciation (~18–11 ka BP)^{22,23}. Yet, it remains unknown regarding the respective roles of biological and solubility pump changes in affecting these past surface-water $p\text{CO}_2$ rises in the SAZ and by extension atmospheric $p\text{CO}_2$ changes.

Here, we systematically investigate the contributions of the biological and solubility pumps to the SAZ surface-water $p\text{CO}_2$ changes in the modern ocean and during the last deglaciation. For the deglacial investigation, we have generated a surface-water $p\text{CO}_2$ record using a sediment core from the Southwest Pacific, paired with nutrient utilization efficiency and sea surface temperature (SST) reconstructions. We evaluate the relative roles of biological and solubility pumps in regulating deglacial surface-water $p\text{CO}_2$ changes at our site location. The same approach is further applied to published records at three additional SAZ locations. Moreover, we examine simulated early deglacial carbon cycle changes in an earth system model²⁸ to distinguish effects of the two pumps during the early deglaciation. All our investigations suggest a strong solubility pump effect on the SAZ surface-water $p\text{CO}_2$ changes, urging a rethinking of mechanisms underlying deglacial CO_2 outgassing from the SAZ and, by extension, past atmospheric $p\text{CO}_2$ variabilities.

Results

Solubility pump in the modern SAZ

In the modern SAZ, both biological and solubility pumps strongly control spatial distribution and seasonal variability of surface-water $p\text{CO}_2$ ^{12,13,29}. Regarding the spatial distribution, Fig. 1a shows small northward declines in annual mean surface-water $p\text{CO}_2$ within the SAZ, where nutrient (nitrate) is progressively utilized equatorward (Fig. 1b). Enhanced nutrient consumption would lower surface-water $p\text{CO}_2$, but this biological effect is compensated by the opposing influence of equatorward surface-water warming in the SAZ (Fig. 1c). Consequently, surface-water $p\text{CO}_2$ changes caused by nutrient consumption is largely balanced by decreasing CO_2 solubility, and the total northward surface-water $p\text{CO}_2$ decline is marginal. Regarding the seasonal variability, Fig. 1d shows minimal monthly surface-water $p\text{CO}_2$ deviation from the annual mean levels in the SAZ. By contrast, seasonal changes in the biological and solubility pumps each cause surface-water $p\text{CO}_2$ to fluctuate ~40 ppm around the annual mean level (Fig. 1e, f)^{12,29}. Because the strong (weak) biological pump occurs during warm (cold) seasons with low (high) CO_2 solubility, effects from the biological and solubility pumps generally cancel each other, leading to little seasonal surface-water $p\text{CO}_2$ variability. Combined, these spatial and temporal patterns suggest that the solubility pump plays a critical role, comparable to that of the biological pump, in determining the SAZ surface-water $p\text{CO}_2$ fluctuations in the modern ocean. Next, we move on to explore the impact of the solubility pump on past surface-water $p\text{CO}_2$ changes, a topic that has rarely been studied by proxy reconstructions.

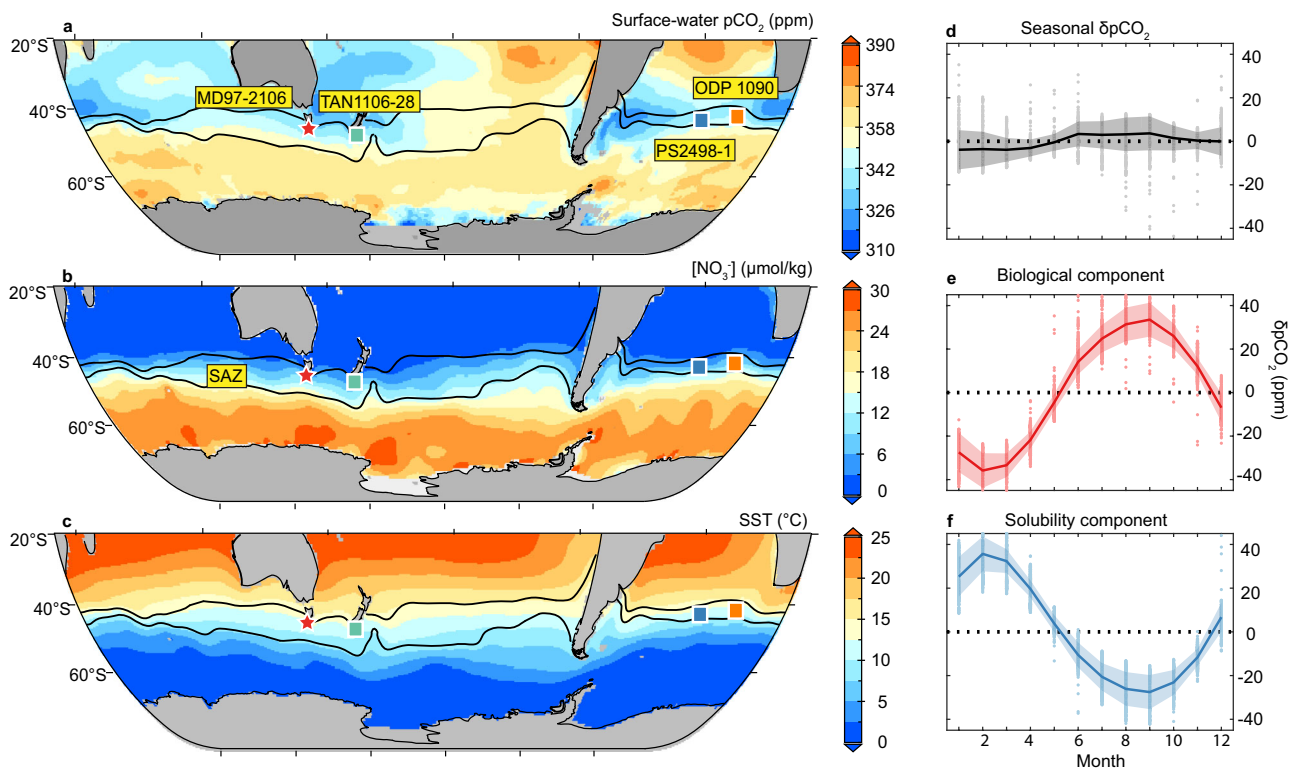


Fig. 1 | Surface-water chemistry in the modern Southern Ocean. **a** Annual mean surface-water $p\text{CO}_2$ during years 1985–2018. The map is made from data presented in Gregor and Gruber²⁹, <https://creativecommons.org/licenses/by/4.0/>. **b** Annual mean surface-water nitrate concentration. The map is made from data presented in Garcia et al.⁴⁸, accessible from <https://www.ncei.noaa.gov/access/world-ocean-atlas-2018/>. **c** Annual mean sea surface temperature. Two black curves indicate the modern positions of the Subtropical Front (STF; the northern curve) and the Subantarctic Front (SAF; the southern curve), respectively, and the region between them is the Subantarctic Zone (SAZ). The red star represents the location of our study site MD97-2106, and squares represent locations with published $\delta^{11}\text{B}$ -based surface-water $p\text{CO}_2$ reconstructions in the SAZ. The map is

made from data presented in Locarnini et al.⁴⁹, accessible from <https://www.ncei.noaa.gov/access/world-ocean-atlas-2018/>. **d** Monthly surface-water $p\text{CO}_2$ variability within the SAZ (year 1985–2018) calculated from the OceanSODA-ETHZ dataset²⁹. **e** Monthly surface-water $p\text{CO}_2$ variability attributed to biological pump changes within the SAZ calculated from the OceanSODA-ETHZ dataset²⁹. **f** Monthly surface-water $p\text{CO}_2$ variability attributed to solubility pump changes within the SAZ calculated from the OceanSODA-ETHZ dataset²⁹. In **d–f**, shadings show $\pm 1\sigma$ standard deviation ranges of observations at discrete locations (represented by dots). As can be seen from **d–f**, the solubility pump plays a critical role in stabilizing SAZ surface-water $p\text{CO}_2$ by countering effects due to biological pump changes.

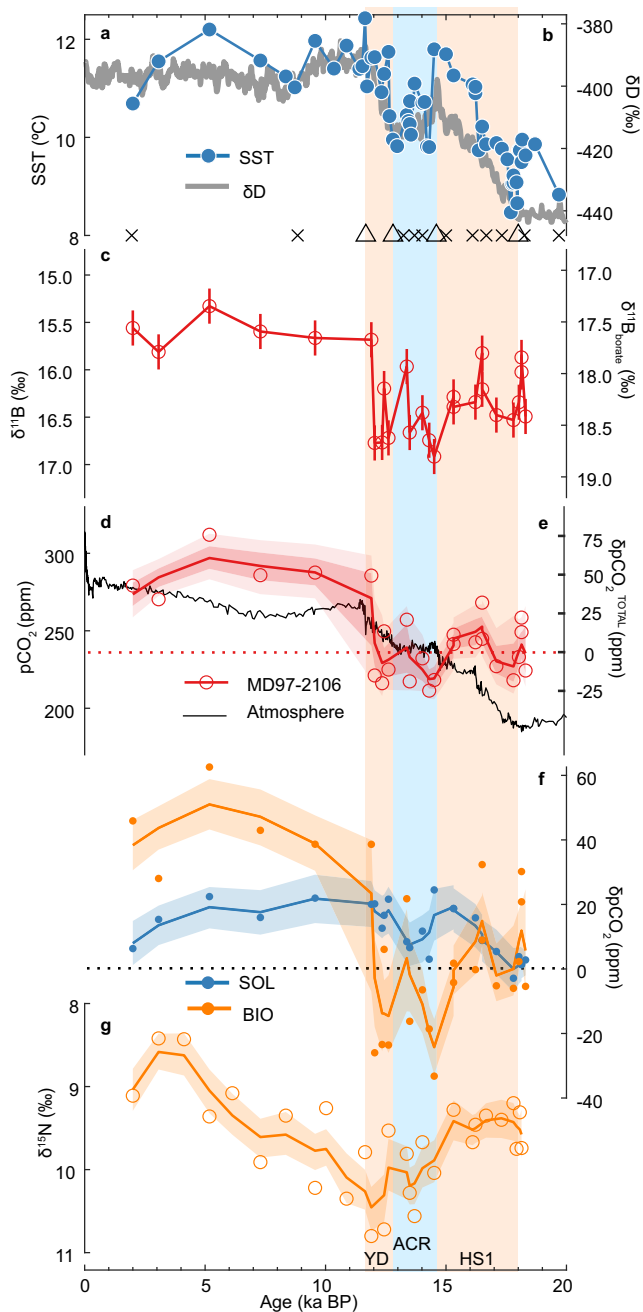


Fig. 2 | Surface-water reconstructions at site MD97-2106. a Sea surface temperature (SST) reconstructed from planktic foraminiferal Mg/Ca³⁶ (blue circles, left axis). **b** Antarctic temperature changes represented by δD^{26} (gray curve, right axis). Crosses and triangles at the bottom are age control points based on planktic radiocarbon dating and SST- δD matching, respectively. **c** Planktic foraminiferal $\delta^{11}B$ and seawater borate $\delta^{11}B$ with error bars showing $\pm 2\sigma$ uncertainties. **d** Reconstructed surface-water pCO_2 at site MD97-2106 (red circles) compared with atmospheric pCO_2 recorded in the Antarctic ice cores (black curve)^{43,44} (left axis). **e** Total surface-water pCO_2 change relative to 18 ka (δpCO_2^{TOTAL}) at site MD97-2106 (right axis). **f** Deglacial surface-water pCO_2 attributed to the solubility and biological pumps (δpCO_2^{SOL} and δpCO_2^{BIO} , blue and orange dots, respectively) at site MD97-2106. **g** Foraminifera-bound $\delta^{15}N$, a proxy reflecting surface nutrient utilization. Curves in **d–g** are derived from a LOESS smoother. In **d**, light and dark envelopes, respectively, represent 2.3–97.7% (roughly $\pm 2\sigma$) and 15.9–84.1% (roughly $\pm 1\sigma$) uncertainty ranges of timeseries incorporating uncertainties from measurements, all individual parameters used for calculations, and age models. In **f** and **g** only 15.9–84.1% uncertainty ranges are shown for clarity. The vertical pale orange bars represent Heinrich Stadial 1 (HS1; -18.0–14.6 ka BP) and the Younger Dryas (YD; -12.8–11.7 ka BP). The vertical pale blue bar represents the Antarctic Cold Reversal (ACR; -14.6–12.8 ka BP). δpCO_2^{SOL} and δpCO_2^{BIO} (**f**) show similar structures to SST (**a**) and foraminifera-bound $\delta^{15}N$ (**g**), respectively.

radiocarbon dates and tuning of SST at this site to Antarctic temperatures²⁶ (Fig. 2a, b; Supplementary Table 1, Supplementary Fig. 4). See Methods for analytical details.

Our reconstructed surface-water pCO_2 at site MD97-2106 fluctuated between -210 and -270 ppm during the last deglaciation, reached -270 ppm at the onset of the Holocene, and increased by -20 ppm from the early to middle Holocene (Fig. 2d). The range of deglacial surface-water pCO_2 at site MD97-2106 is comparable to previous reconstructions^{22,23}. At our site, surface-water pCO_2 briefly dropped below the atmospheric pCO_2 values during the Antarctic Cold Reversal (ACR; 14.6–12.8 ka BP) and the Younger Dryas (YD; 12.8–11.7 ka BP) (Fig. 2d).

In addition to our surface-water pCO_2 reconstructions, we employ $\delta^{15}N_{FB}$ to infer nitrate utilization efficiency at site MD97-2106. $\delta^{15}N_{FB}$ reflects $\delta^{15}N$ of surface-water nitrate taken up by foraminifera which increases as surface nitrate is progressively consumed by photosynthetic algae^{11,37,38}. During Heinrich Stadial 1 (HS1; 18.0–14.6 ka BP) when the age model of our core is well constrained by a warming phase, $\delta^{15}N_{FB}$ at our site remained roughly unchanged (Fig. 2b, g). This observation is consistent with a precisely dated coral-bound $\delta^{15}N$ record from the same region showing minimal $\delta^{15}N$ variability over the same period²¹ (Supplementary Fig. 9). Maxima of $\delta^{15}N_{FB}$ occurred during the ACR and the YD, coinciding with surface-water pCO_2 minima. During the Holocene, $\delta^{15}N_{FB}$ declined by about 2.0‰, consistent with other fossil-bound $\delta^{15}N$ records from the Southern Ocean^{11,21,39–41}.

New deglacial SAZ surface-water pCO_2 and $\delta^{15}N$ records

We present records of surface-water pCO_2 and nutrient utilization, respectively, based on boron isotopes ($\delta^{11}B$)^{22,30,31} and foraminifera-bound nitrogen isotopes ($\delta^{15}N_{FB}$) of mixed-layer-dwelling planktic foraminifera species *Globigerina bulloides* for site MD97-2106 from the Southwest Pacific Ocean (Fig. 1). Site MD97-2106 (45.15°S, 146.28°E) is located in the northern part of the SAZ. Compared to today, the Subtropical Front, the northern boundary of the SAZ, possibly shifted northward to Tasmania during the Last Glacial Maximum (LGM; -22–18 ka)^{32,33}. During the last deglaciation, the Subtropical Front might migrate southwards^{32,33}, but unlikely to the south of our site. This is because the Subtropical Front marks a -4 °C SST gradient³⁴, while reconstructions at our site only show -3 °C SST change during the entire deglaciation^{35,36}. Consequently, our site was likely located within the SAZ during the entire last deglaciation, ideal for investigating deglacial SAZ surface conditions. The age model of site MD97-2106 during the last deglaciation is based on new

Evaluating past biological and solubility effects at site MD97-2106

We partition surface-water pCO_2 changes at site MD97-2106 into two components caused by changes in biological and solubility pumps, using a similar method previously applied to investigate modern surface-water pCO_2 variability^{12,16,29}. Firstly, we calculate total in-situ surface-water pCO_2 changes (noted as δpCO_2^{TOTAL}) relative to the reference age of 18 ka; choosing a different reference age has little effect on our conclusions (Supplementary Fig. 6). Secondly, surface-water pCO_2 is recalculated using carbonate chemistry (i.e., DIC and alkalinity) fixed at the reference age, but using varying SST and sea surface salinity (SSS) based on our reconstructions (Methods). Thirdly, this recalculated surface-water pCO_2 is used to compute changes relative to 18 ka (the reference age). The relative surface-water pCO_2 changes calculated in this way are only driven by SST and SSS, and thus are attributed to the solubility pump effect (noted as δpCO_2^{SOL}). Fourthly, we calculate the difference between δpCO_2^{TOTAL} and δpCO_2^{SOL} , which is defined as the

biology-driven surface-water $p\text{CO}_2$ change (noted as $\delta p\text{CO}_2^{\text{BIO}}$). We also provide an alternative approach to directly calculate $\delta p\text{CO}_2^{\text{BIO}}$, which yields consistent results with those presented in the main text (Methods; Supplementary Fig. 8). Any influence of external processes on surface-water $p\text{CO}_2$, such as changes associated with frontal shift, is embedded in our method, because these external processes affect surface-water $p\text{CO}_2$ via the carbonate chemistry, SST-SSS, or both. See “Methods” for calculation details.

As can be seen from Fig. 2f, $\delta p\text{CO}_2^{\text{BIO}}$ at site MD97-2106 fluctuated between -20 ppm and $+40$ ppm from the LGM to the early Holocene, followed by a -20 -ppm increase during the Holocene. From 18 to 15 ka, $\delta p\text{CO}_2^{\text{BIO}}$ showed little net change, suggesting marginal influence of biological processes on surface-water $p\text{CO}_2$ variations at our site. During the ACR and the YD, $\delta p\text{CO}_2^{\text{BIO}}$ exhibits mostly negative values, indicating a strengthened biological pump that would lower surface-water $p\text{CO}_2$ during these times. The evolution of $\delta p\text{CO}_2^{\text{BIO}}$ at our site is well corroborated by our $\delta^{15}\text{N}_{\text{FB}}$ record from the same core. Little net $\delta p\text{CO}_2^{\text{BIO}}$ change concurred with stable $\delta^{15}\text{N}_{\text{FB}}$ during HSI, while negative $\delta p\text{CO}_2^{\text{BIO}}$ during the ACR and the YD coincided with higher $\delta^{15}\text{N}_{\text{FB}}$ values which indicate more complete nutrient utilization (Fig. 2f–g). We note that, in addition to nitrate utilization in the SAZ, our $\delta^{15}\text{N}_{\text{FB}}$ might have also been affected by $\delta^{15}\text{N}$ of nitrate supplied to our site, which depends on the nitrate utilization of the nitrate source^{11,21,41,42}. Despite these complications, similar deglacial structures in $\delta^{15}\text{N}_{\text{FB}}$ and independently derived $\delta p\text{CO}_2^{\text{BIO}}$ suggest that $\delta^{15}\text{N}_{\text{FB}}$ at site MD97-2106 reflects local nitrate utilization efficiency. Moreover, given their independent methods, consistent patterns of our $\delta p\text{CO}_2^{\text{BIO}}$ and $\delta^{15}\text{N}_{\text{FB}}$ lend strong support to our inference about past biological pump changes at this site. In stark contrast to previous findings in the SAZ^{22–24}, our $\delta p\text{CO}_2^{\text{BIO}}$ and $\delta^{15}\text{N}_{\text{FB}}$ suggest that the biological pump played a minor role in contributing to surface-water $p\text{CO}_2$ and thus air-sea CO_2 exchange at site MD97-2106 during HSI and the YD when atmospheric $p\text{CO}_2$ rose substantially^{43,44}.

Compared with $\delta p\text{CO}_2^{\text{BIO}}$, our calculated $\delta p\text{CO}_2^{\text{SOL}}$, which reflects solubility pump effects, shows a different history (Fig. 2f). As expected, deglacial $\delta p\text{CO}_2^{\text{SOL}}$ increased in response to warming, although this warming effect was slightly counteracted by a declining SSS (Supplementary Fig. 5). From 18 to 10 ka, $\delta p\text{CO}_2^{\text{SOL}}$ showed a net increase of -20 ppm, contributing to about one-third of the $\delta p\text{CO}_2^{\text{TOTAL}}$ at site MD97-2106 over the same period. More specifically, the $\delta p\text{CO}_2^{\text{SOL}}$ increase dominated the $\delta p\text{CO}_2^{\text{TOTAL}}$ rise from 18 to 15 ka, in contrast to little net change in the concurrent $\delta p\text{CO}_2^{\text{BIO}}$. This highlights the critical role of the weakened solubility pump in maintaining positive sea-air $p\text{CO}_2$ gradients, which would contribute to the atmospheric $p\text{CO}_2$ rise during HSI. During the YD, rising $\delta p\text{CO}_2^{\text{SOL}}$ helped reverse biological effects (shown by $\delta p\text{CO}_2^{\text{BIO}}$ and $\delta^{15}\text{N}_{\text{FB}}$) to limit the development of negative sea-air $p\text{CO}_2$ gradient (Fig. 2f–g), contributing to the contemporary atmospheric $p\text{CO}_2$ rise.

By separating influences of the biological and solubility pumps downcore, we demonstrate that a substantial portion of deglacial surface-water $p\text{CO}_2$ rise at our site originated from variations in the solubility pump. This suggests that the solubility pump, which has been neglected in previous investigations in the region, played an important role in regulating deglacial surface-water $p\text{CO}_2$ changes in the Pacific SAZ.

Proxy and model data evaluation for broader SAZ

To quantify past influences of biological and solubility pumps in broader SAZ regions, we reanalyze deglacial surface-water $p\text{CO}_2$ changes at three additional locations using published proxy records^{22,23} (Figs. 1a; 3b–d). At all the investigated sites, our calculated $\delta p\text{CO}_2^{\text{BIO}}$ suggests little-to-modest biological pump effects on SAZ surface-water $p\text{CO}_2$ during times with large atmospheric $p\text{CO}_2$ rises. For instance, except for a brief excursion at -17 ka, $\delta p\text{CO}_2^{\text{BIO}}$ at Site ODP 1090 (Fig. 3b) varied little and suggests minimal biological pump

effects on surface-water $p\text{CO}_2$ during the last deglaciation²³. At site PS2498-1, despite an overall larger $\delta p\text{CO}_2^{\text{BIO}}$ contribution to surface-water $p\text{CO}_2$ compared to other sites, roughly stable average $\delta p\text{CO}_2^{\text{BIO}}$ during -14 – 11 ka contributed little to the observed surface-water $p\text{CO}_2$ rise (Fig. 3c). At site TAN1106-28, $\delta p\text{CO}_2^{\text{BIO}}$ showed a prominent peak at -16 ka, but the general deglacial trend of $\delta p\text{CO}_2^{\text{BIO}}$ is poorly defined by the low temporal resolution. In contrast to $\delta p\text{CO}_2^{\text{BIO}}$ changes, our calculated $\delta p\text{CO}_2^{\text{SOL}}$ at all studied sites supports that solubility pump changes consistently contributed to deglacial $\delta p\text{CO}_2^{\text{TOTAL}}$. From 18 to 10 ka, we observe well-defined $\delta p\text{CO}_2^{\text{SOL}}$ increases of -20 ppm at Site ODP 1090 from the South Atlantic. At site TAN1106-28 from the South Pacific, $\delta p\text{CO}_2^{\text{SOL}}$ increased by -50 ppm, in response to the deglacial SST change of -7 °C in part caused by a possible frontal shift over this site²³. Although the record at site PS2498-1 does not cover the entire last deglaciation, $\delta p\text{CO}_2^{\text{SOL}}$ at this site shows a -30 -ppm increase during -14 – 11 ka (Fig. 3c). These $\delta p\text{CO}_2^{\text{SOL}}$ changes significantly contribute to, or even dominate, the surface-water $p\text{CO}_2$ variations at these sites, strengthening our findings at site MD97-2106. Overall, our analyses of proxy data from different sectors of the Southern Ocean demonstrate that deglacial surface-water $p\text{CO}_2$ changes in the SAZ are substantially affected by solubility pump changes, rather than solely by biological pump changes as previously assumed^{11,22,23}.

We further scrutinize the role of the solubility pump in affecting deglacial SAZ surface-water $p\text{CO}_2$ in a simulation by climate model LOVECLIM²⁸. In this simulation, a 30-ppm atmospheric $p\text{CO}_2$ increase is achieved during HSI when the Southern Ocean overturning circulation and southern hemisphere westerly winds are intensified. The rising surface-water $p\text{CO}_2$ in the Southern Ocean is diagnosed as a main CO_2 source for the early deglacial atmospheric $p\text{CO}_2$ increase²⁸. Using the same method applied to proxy data, we quantify $\delta p\text{CO}_2^{\text{BIO}}$ and $\delta p\text{CO}_2^{\text{SOL}}$ changes between 19 ka and 15 ka in this simulation (“Methods”). Our decomposition (Fig. 4) reveals that $\delta p\text{CO}_2^{\text{BIO}}$ changes are either small or tend to lower $p\text{CO}_2^{\text{TOTAL}}$ in the SAZ. Because nutrient utilization forced by iron availability is not prescribed in the model, our calculated $\delta p\text{CO}_2^{\text{BIO}}$ per se cannot be used to dismiss iron fertilization effect on deglacial SAZ surface-water $p\text{CO}_2$ changes. By contrast, $\delta p\text{CO}_2^{\text{SOL}}$ changed substantially due to strong surface warming, dominating surface-water $\delta p\text{CO}_2^{\text{TOTAL}}$ rise in the SAZ (Fig. 4). Therefore, our model data analyses suggest that solubility pump changes are crucial for deglacial surface-water $p\text{CO}_2$ and air-sea CO_2 exchange in the SAZ, strengthening our findings based on above extensive proxy reconstructions.

Discussion

It is widely thought that declined biological pump efficiency, possibly owing to reducing nutrient utilization associated with dust-borne iron deposition, enhanced CO_2 outgassing in the SAZ and hence atmospheric $p\text{CO}_2$ rises during deglaciations^{1,10,11,24}. During HSI when atmospheric $p\text{CO}_2$ raised substantially and dust deposition in Antarctica declined dramatically⁴⁵ (Fig. 3), $\delta p\text{CO}_2^{\text{BIO}}$, together with independently measured $\delta^{15}\text{N}_{\text{FB}}$, indicates little net biological pump change at site MD97-2106. Over the same period, $\delta p\text{CO}_2^{\text{BIO}}$ shows little increase in response to the reduced iron fertilization inferred from dust deposition in Antarctica⁴⁵ and other examined sites. At two of the examined sites (ODP 1090 and PS2498-1), where opal and lithogenic fluxes are available^{24,46–48}, $\delta p\text{CO}_2^{\text{BIO}}$ shows correlation with neither flux during HSI^{24,46,47} (Fig. 3b, c). In addition to local nutrient utilization efficiency, $\delta p\text{CO}_2^{\text{BIO}}$ and $\delta^{15}\text{N}_{\text{FB}}$ at a certain site in the SAZ may also be affected by nutrient supplies modulated by shifts of the Southern Ocean fronts^{11,21,39,41,42}. Everything else being equal, poleward movements of the Subtropical and Subantarctic fronts and thus the SAZ during HSI would reduce nutrient supply, with an effect to raise observed nutrient utilization efficiency, at any given location in the SAZ. During HSI, declining local nutrient utilization efficiency deduced from reduced iron fertilization and poleward front shifts would have

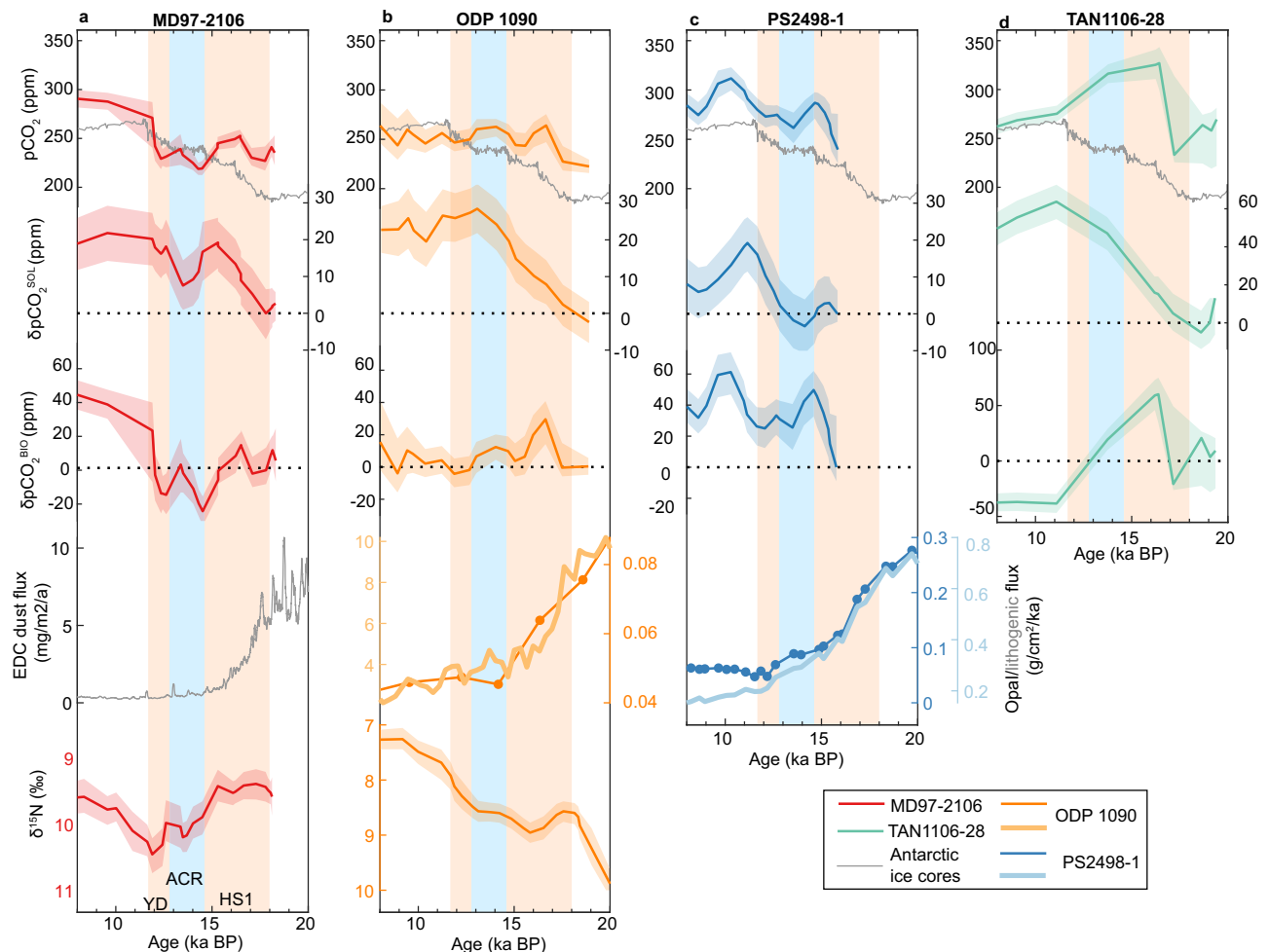


Fig. 3 | Deglacial surface-water $p\text{CO}_2$, solubility and biological pump effects, dust and opal fluxes, and nutrient utilization at four Subantarctic Zone sites. **a** MD97-2106; **b** ODP 1090^{11,23,46}; **c** PS2498-1^{22,47}; and **d** TAN1106-28²³. Data in the four panels are arranged as follows. First row: surface-water $p\text{CO}_2$ at investigated sites (red, orange, blue, and green curves) compared to atmospheric $p\text{CO}_2$ recorded in Antarctic ice cores^{43,44} (gray curves). Second row: surface-water $p\text{CO}_2$ change attributed to the solubility pumps ($\delta p\text{CO}_2^{\text{sol}}$). Third row: surface-water $p\text{CO}_2$ change attributed to the biological pump ($\delta p\text{CO}_2^{\text{bio}}$). Fourth row: dust fluxes recorded in an Antarctic ice core⁴⁵ (i), lithogenic (pale orange curve)²² and opal (orange curve with dots)⁴⁶ fluxes at site ODP 1090 (**b**), lithogenic (pale blue curve) and opal (blue curve with dots) fluxes at site PS2498-1⁴⁷ (**c**). Fifth row: Foraminifera-bound $\delta^{15}\text{N}$ (this study and¹¹). Note that scales of $\delta p\text{CO}_2^{\text{sol}}$ and $\delta p\text{CO}_2^{\text{bio}}$ differ in

d compared to **a–c**. Envelopes represent 15.9–84.1% uncertainties incorporating uncertainties from measurements, all individual parameters required for calculations, and age models. The vertical pale orange bars represent Heinrich Stadial 1 (HS1; -18.0–14.6 ka BP) and the Younger Dryas (YD; -12.8–11.7 ka BP). The vertical pale blue bar represents the Antarctic Cold Reversal (ACR; -14.6–12.8 ka BP). The reference age for relative surface-water $p\text{CO}_2$ change decomposition at these sites is set at 18 ka, except at site PS2498-1, where it is set at the oldest age of -15.8 ka. For all sites examined, solubility pump changes consistently contribute -20–50 ppm to the deglacial surface-water $p\text{CO}_2$ changes (second row). Surface-water $p\text{CO}_2$ changes attributed to the biological pump (third row) differ from dust and export production (fourth row).

opposing effects on SAZ $\delta p\text{CO}_2^{\text{bio}}$, and their combined effects may result in minimal $\delta p\text{CO}_2^{\text{bio}}$ changes overall. Thus, despite the lack of any $\delta p\text{CO}_2^{\text{bio}}$ decline, our reconstructions imply a potential role of iron fertilization in affecting surface-water $p\text{CO}_2$ through nutrient utilization in the SAZ during HS1.

Instead of a dominant biological contribution, our systematic investigations reveal persistent influences of the solubility pump on surface-water $p\text{CO}_2$ fluctuations in the SAZ under both modern and past conditions. Modern hydrographical data shows that the solubility pump causes surface-water $p\text{CO}_2$ to fluctuate by ~40 ppm seasonally (Fig. 1). New and published proxy data demonstrates a solubility effect that can modulate surface-water $p\text{CO}_2$ by -20–50 ppm on millennial timescales during the last deglaciation (Figs. 2 and 3). The strong solubility pump influence is likely widespread in the SAZ, as shown by >20 ppm surface-water $p\text{CO}_2$ increase attributable to solubility pump changes during the early deglaciation in a model simulation²⁸ (Fig. 4). Notably, in this model simulation, solubility pump changes in the SAZ

lead to strong CO_2 outgassing and, together with other Southern Ocean processes, contribute to a full-scale atmospheric $p\text{CO}_2$ increase during HS1 without invoking nutrient utilization efficiency changes related to iron fertilization²⁸. Based on our analyses on modern data, proxy reconstructions, and modeling outputs, we suggest that a weakened solubility pump, driven by warming, contributed critically to the rising surface-water $p\text{CO}_2$ in the SAZ and thereby maintaining this region as a CO_2 source to the atmosphere during the last deglaciation.

In sum, while our $\delta p\text{CO}_2^{\text{bio}}$ reconstructions, at face value, indicate little biological pump contributions to deglacial SAZ surface-water $p\text{CO}_2$ variations at various SAZ sites locally, these reconstructions imply iron-related nutrient utilization effects on the deglacial SAZ surface-water $p\text{CO}_2$ variabilities when the influence of frontal shift is considered. Nevertheless, such an iron-related biological effect appears to be smaller than previously thought. Therefore, the common view that the iron-regulated SAZ biological pump changes substantially contributed to the deglacial atmospheric $p\text{CO}_2$ rise^{8–11} may

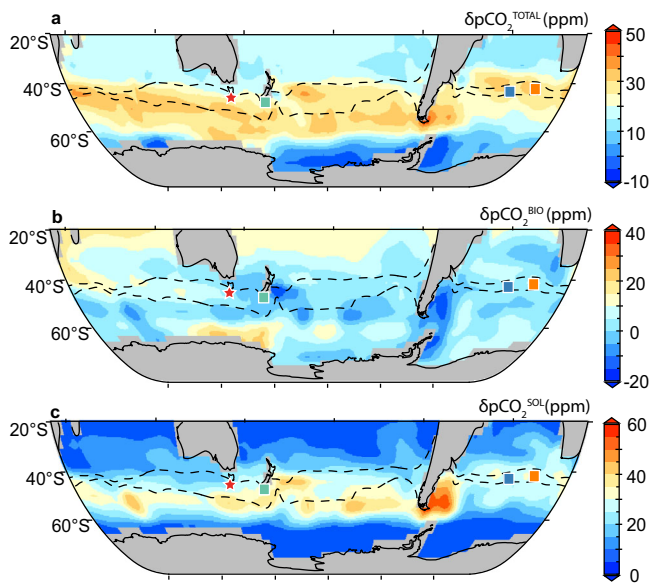


Fig. 4 | Southern Ocean surface-water pCO₂ changes in a climate model simulation during the last deglaciation²⁸. **a** Total surface-water pCO₂ change ($\delta p\text{CO}_2^{\text{TOTAL}}$). **b** surface-water pCO₂ change attributed to the biological pump ($\delta p\text{CO}_2^{\text{BIO}}$). **c**, surface-water pCO₂ change attributed to the solubility pump ($\delta p\text{CO}_2^{\text{SOL}}$). All anomalies (δ) represent changes between 19 ka and 15 ka. Note different $\delta p\text{CO}_2$ scales for the three panels. The region between the dotted lines is the modern Subantarctic Zone (SAZ). The locations of MD97-2106 (red star) and other investigated sites (ODP 1090, orange square; PS2498-1, blue square; TANI106-28 teal square) are shown. As can be seen, the total $\delta p\text{CO}_2^{\text{TOTAL}}$ rise in the SAZ from 19 to 15 ka in this model simulation is mainly driven by solubility pump changes. The figure is made from recalculation based on data presented in Menviel et al.²⁸.

need to be re-evaluated. In comparison to the widely recognized biological pump effect, the potential effect of the solubility pump in the SAZ has been previously overlooked when explaining the past atmospheric pCO₂ changes. Our work demonstrates that the solubility pump plays an indispensable role in modulating SAZ surface-water pCO₂ under both modern and past conditions. We suggest future works on quantifying the effect of SAZ solubility pump on past and possibly future atmospheric pCO₂ changes, which would have important implications for our mechanistic understanding of the global carbon cycle.

Methods

Trace element and boron isotope analyses

About 30 to 40 shells of planktic foraminifera *G. bulloides* from the 300–355 μm size fraction and >5 mg of *G. bulloides* shells from the 250–355 μm size fraction were picked for trace element and $\delta^{11}\text{B}$ analyses, respectively. These samples were cleaned following the “Mg-cleaning” procedure^{50–53}. Measurements of B/Ca and Mg/Ca, along with Al/Ca and Mn/Ca for monitoring contaminants, were performed on an iCAP Inductively coupled plasma-mass spectrometry (ICP-MS) at the Australian National University (ANU), following an established method⁵¹.

Separation of boron from sample matrices and measurement of $\delta^{11}\text{B}$ on a multi-collector-ICP-MS (MC-ICP-MS) generally follows the method of Foster³¹ with some modifications. The cleaned foraminifera shells were dissolved in 0.5 M HNO₃, and buffered by 2 M NH₄Ac, instead of NaAc-HAc mixture, to pH of -5.5. We changed the buffering solution to eliminate potential matrix contamination of Na on the $\delta^{11}\text{B}$ measurement. The buffered solution was gravitationally dripped into micro-columns, loaded with 20 μL ion exchange resin (Amberlite IRA-743, 63–125 μm size fraction), which was pre-cleaned by 0.5 M HNO₃

and then boron-free deionized water. These micro-columns were tested by processing reference materials (boric acid solutions, NIST SRM 951 and ERM AE-121, without and with addition of CaCO₃ matrix; standard carbonates, NEP-3B) and generating values consistent with published values. After rinsing the resin eight times using Milli-Q water, boron was eluted by five aliquots of 90 μL 0.5 M HNO₃. A sixth aliquot was also added and collected to check for complete boron recovery. Total procedure blanks for each batch of samples were monitored, and were between -20 and 100 pg.

$\delta^{11}\text{B}$ was measured on a MC-ICP-MS (Neptune Plus) at ANU using a standard bracketing method similar to Foster²⁹. Following Farmer et al.⁵⁴, we measured boron blanks before every bracketing standard (NIST SRM 951) and sample. We also introduce water aerosol into the spray chamber through a second nebulizer after every standard/sample measurement in addition to the routine rinse, to flush out boron in order to minimize the memory effect of boron. An analytical block is as follows: flush-blank-standard-flush-blank-sample-flush-blank-standard. With the additional water flushing in between, measured blanks for ^{11}B can be kept <1.8% (an average for blanks of all the samples, external standards, and bracketing standards during 5 sessions) of the bracketing standard with 30 ppb of boron. Prior to and during analyses of these samples, repeating measurements of standard materials (NIST SRM 951, ERM AE-121, NEP-3B, and NIST RM 8301f) yield results consistent with their published values (Supplementary Table 2). The external reproducibility is estimated by repeating measurements of standard ERM AE-121 at 30-ppb boron concentration along with the samples ($2\sigma = 0.17\%$, $n = 12$). The boron concentration of the standard is chosen to match the expected median concentration of samples. Three of the foraminiferal samples were divided into two subsamples and processed separately from the cleaning step, and standard deviations of these replicated samples range from 0.08 to 0.27‰ (Supplementary Table 3).

During the late LGM and HSI, *G. bulloides* $\delta^{11}\text{B}$ we measured at site MD97-2106 agrees with previous measurements by MC-ICP-MS in the Pacific and Atlantic SAZ²³ and the Subtropical Southwest Pacific⁵⁵, but is on average -1‰ lower than those from the same site measured on a Negative Thermal Ionization Mass Spectrometry (N-TIMS) by a previous study⁵⁶ (Supplementary Fig. 3). We tentatively attribute such offsets to potential analytical biases between MC-ICP-MS and N-TIMS that, as shown by a previous study, range from 0.5 to 2.7‰ and appear to enlarge for samples with low B/Ca values⁵⁴. Despite that Moy et al.⁵⁶ show different deglacial $\delta^{11}\text{B}$ and thus surface-water pCO₂ magnitudes, deglacial $\delta p\text{CO}_2^{\text{SOL}}$ and $\delta p\text{CO}_2^{\text{BIO}}$ calculated using their data show similar patterns to those based on our new data (Supplementary Fig. 3).

Carbonate chemistry system calculation

G. bulloides $\delta^{11}\text{B}$ is converted into $\delta^{11}\text{B}$ of seawater borate ($\delta^{11}\text{B}_{\text{borate}}$) using the calibration from Raitzsch, et al.³⁰: $\delta^{11}\text{B}_{\text{borate}} = (\delta^{11}\text{B}_{G. \text{bulloides}} + 3.58 \pm 11.77)/(1.09 \pm 0.65)$. To estimate pH, SST and surface seawater salinity (SSS) are required. SST is estimated from *G. bulloides* Mg/Ca using the calibration of Elderfield and Ganssen³⁵. SSS is estimated from the global sea-level change following Foster³¹. To calculate seawater pCO₂, seawater alkalinity is estimated from the modern seawater SSS-alkalinity relation²⁰. We then use the CO2sys script⁵⁷ to calculate seawater pCO₂ and other carbonate chemistry parameters including DIC. The 2.3–97.7% uncertainties of seawater pCO₂ are propagated by a 10,000-iteration Monte-Carlo method incorporating uncertainties from $\delta^{11}\text{B}$ ($2\sigma = 0.17\%$), SST ($2\sigma = 1^\circ\text{C}$), and SSS ($2\sigma = 0.5$), and alkalinity which is sourced from SSS and the modern SSS-alkalinity relation²⁰. Using a different way to estimate alkalinity (Supplementary Fig. 7) does not substantially affect our calculated seawater pCO₂ and its decompositions. For published $\delta^{11}\text{B}$ records, surface-water pCO₂ is recalculated using the same method as this study to be consistent with our methodology. Final uncertainties shown in Figs. 2 and 3 also

incorporate age uncertainties. For site MD97-2106, age uncertainty (1 σ ranging from 0.2 to 0.8 ka) is derived from the Undatable script³⁸, and for published records, a uniform age uncertainty (1 σ) of 0.5 ka is assigned.

We partition the total in-situ surface-water pCO₂ changes ($\delta p\text{CO}_2^{\text{TOTAL}}$) into two components: solubility-driven ($\delta p\text{CO}_2^{\text{SOL}}$) and biology-driven ($\delta p\text{CO}_2^{\text{BIO}}$) components. In the main text, $\delta p\text{CO}_2^{\text{SOL}}$ is derived first, and the difference between $\delta p\text{CO}_2^{\text{TOTAL}}$ and $\delta p\text{CO}_2^{\text{SOL}}$ is defined as $\delta p\text{CO}_2^{\text{BIO}}$. Here, we provide an alternative method to derive $\delta p\text{CO}_2^{\text{BIO}}$ first and subsequently $\delta p\text{CO}_2^{\text{SOL}}$. Firstly, $\delta p\text{CO}_2^{\text{TOTAL}}$ is calculated the same way as described in the main text. Secondly, we use DIC and alkalinity values (the same as those used for in-situ pCO₂ calculations), but constant SST and SSS values at 18 ka to calculate new surface-water pCO₂. It is important to note that DIC and alkalinity are used as intermediate parameters for calculations, and their values do not need to be accurately quantified to yield well-quantified new pCO₂ values. This is because DIC and alkalinity are inherently linked given constraint from pH (see Yu et al.⁵⁹ for detailed discussions). Thirdly, $\delta p\text{CO}_2^{\text{BIO}}$ is calculated by changes in the newly calculated surface-water pCO₂ relative to 18 ka. Fourthly, $\delta p\text{CO}_2^{\text{SOL}}$ is defined by differencing $\delta p\text{CO}_2^{\text{TOTAL}}$ and $\delta p\text{CO}_2^{\text{BIO}}$. As can be seen from Supplementary Fig. 8, the two methods yield consistent results, strengthening reliability of our calculation. The small differences between these two methods are due to the non-linear responses of seawater pCO₂ to temperature and DIC changes.

For $\delta p\text{CO}_2^{\text{SOL}}$, it may be further partitioned into temperature- and salinity-driven components ($\delta p\text{CO}_2^{\text{T}}$ and $\delta p\text{CO}_2^{\text{S}}$, respectively). We first calculate new surface-water pCO₂ at each age by using constant DIC, alkalinity, and SSS at 18 ka, but varying SST. Then, $\delta p\text{CO}_2^{\text{T}}$ is derived as changes of the newly calculated pCO₂ relative to 18 ka. Afterward, $\delta p\text{CO}_2^{\text{S}}$ is defined as the difference between $\delta p\text{CO}_2^{\text{SOL}}$ and $\delta p\text{CO}_2^{\text{T}}$. As can be seen from Supplementary Fig. 5, salinity changes tend to counter temperature effect on pCO₂, but $\delta p\text{CO}_2^{\text{S}}$ are limited to within 10 ppm at all four SAZ sites studied.

Regarding model outputs²⁸, we first calculate $\delta p\text{CO}_2^{\text{TOTAL}}$ between 15 ka and 19 ka, simply by differencing in-situ surface-water pCO₂ values at these times ($p\text{CO}_2^{\text{in-situ,15ka}}$ and $p\text{CO}_2^{\text{in-situ,19ka}}$, respectively). We re-calculate surface-water pCO₂ at 15 ka ($p\text{CO}_2^{\text{recalc,15ka}}$) using DIC and alkalinity at 15 ka but using SST and SSS at 19 ka. Similar to proxy data, $\delta p\text{CO}_2^{\text{BIO}}$ and $\delta p\text{CO}_2^{\text{SOL}}$ are calculated by: $\delta p\text{CO}_2^{\text{BIO}} = p\text{CO}_2^{\text{recalc,15ka}} - p\text{CO}_2^{\text{in-situ,19ka}}$ and $\delta p\text{CO}_2^{\text{SOL}} = p\text{CO}_2^{\text{TOTAL}} - \delta p\text{CO}_2^{\text{BIO}}$.

For modern hydrological data²⁹, monthly $\delta p\text{CO}_2^{\text{TOTAL}}$, $\delta p\text{CO}_2^{\text{BIO}}$, and $\delta p\text{CO}_2^{\text{SOL}}$ represent deviations from annual mean values. $\delta p\text{CO}_2^{\text{TOTAL}}$, $\delta p\text{CO}_2^{\text{BIO}}$, and $\delta p\text{CO}_2^{\text{SOL}}$ are calculated similarly to those for model results described above. For example, monthly $\delta p\text{CO}_2^{\text{BIO}}$ is calculated using monthly alkalinity and DIC but annual mean SST and SSS, while monthly $\delta p\text{CO}_2^{\text{SOL}}$ is calculated using annual mean alkalinity and DIC but with monthly SST and SSS (Fig. S2).

Foraminifera-bound nitrogen isotope analyses

Sample preparation and measurements of $\delta^{15}\text{N}$ follow protocols in Ren et al.⁶⁰. For each sample, >3 mg of *G. bulloides* shells (250–355 μm size fraction) were picked and crushed under a dissecting microscope. Foraminiferal samples were sonicated in an ultrasonic bath for 5 min with 2% polyphosphate solution, treated in bicarbonate-buffered dithionite–citric acid in an 80 °C water bath for 1 h, and added with basic potassium persulfate solution and autoclaved at 121 °C for 1 h. After every cleaning step, samples were rinsed with deionized water. Cleaned samples were dried overnight at 55 °C. Each sample was weighed (~1.5–3.5 mg) into a combusted glass vial and then dissolved in 3 M HCl to release organic N from the calcite shell. Persulfate oxidation reagent (POR, 0.3 g of 3-time-recrystallized basic potassium persulfate and 0.7 g of NaOH dissolved in 100 mL of deionized water) were added to the dissolved samples which were then autoclaved at 121 °C for 1 h to convert organic N to nitrate. The nitrate concentrations of all POR-

oxidized samples were measured to determine N contents after autoclaving using the chemiluminescence method⁶¹. Average N content of the cleaned calcite samples is 3.07 mmol N per gram. Nitrate concentration of POR and its $\delta^{15}\text{N}$ were constrained by two organic standards (US Geological Survey (USGS) 40, $\delta^{15}\text{N} = -4.5\text{‰}$ vs. air; and a laboratory standard, mixture of 6-aminocaproic acid and glycine, $\delta^{15}\text{N} = 5.4\text{‰}$ vs. air) processed along with samples. Nitrate concentration of POR is 0.2 μM , representing 1–3% of the total N in samples.

The denitrifier method was applied to transform dissolved nitrate and nitrite into nitrous oxide (N₂O) gas using a naturally occurring denitrifying bacterial strain, *Pseudomonas chlororaphis*, which lacks an active form of the enzyme N₂O reductase. After degassing of the bacteria for 3 h, 1.5 mL of the bacterial concentrate was added with 5 nmol of samples acidified to pH of 3–7. Two nitrate reference materials (International Atomic Energy Agency NO₃ reference (IAEA-N3), $\delta^{15}\text{N} = 4.7\text{‰}$ vs. air; and USGS 34, $\delta^{15}\text{N} = -1.8\text{‰}$ vs. air) were processed along with samples to monitor the bacterial conversion and were later repeatedly measured between samples to check the stability of the mass spectrometry.

$\delta^{15}\text{N}$ of foraminiferal samples, together with bacterial blanks and organic standards, were determined by gas chromatography and isotope ratio mass spectrometry using a modified SigBench and MAT253 plus⁶². Due to the small sample size and low N content within foraminifera, no duplicates were made for these samples. Our IAEA-N3 and USGS 34 standards yielded standard deviation (1 σ) of 0.06 and 0.07‰, respectively. The standard deviation (1 σ) of the organic standards analyzed with these samples is 0.15‰, agreeing with the long-term variability of in-house carbonate standards using homogenized coral samples ($\pm 0.25\text{‰}$). As a result, we assume that the analytical error for the $\delta^{15}\text{N}_{\text{FB}}$ is 0.25‰ in our new record.

Data availability

All data generated in this study have been deposited in the Zenodo database under access code: <https://doi.org/10.5281/zenodo.6970032>. All data generated in this study are also provided in the Supplementary Information.

Code availability

Codes used to produce Figs. 1 and 4 are available from Y.D. upon request. Mode output data used to produce Fig. 4 is available from <https://doi.org/10.4225/41/5af39aae7960f28>.

References

- Sigman, D. M., Hain, M. P. & Haug, G. H. The polar ocean and glacial cycles in atmospheric CO₂ concentration. *Nature* **466**, 47–55 (2010).
- Sigman, D. M. & Boyle, E. A. Glacial/interglacial variations in atmospheric carbon dioxide. *Nature* **407**, 859–869 (2000).
- Yu, J. et al. Millennial and centennial CO₂ release from the Southern Ocean during the last deglaciation. *Nat. Geosci.* **15**, 293–299 (2022).
- Yu, J. et al. Loss of carbon from the deep sea since the Last Glacial Maximum. *Science* **330**, 1084–1087 (2010).
- Talley, L. D. *Descriptive Physical Oceanography: An Introduction* (Academic Press, 2011).
- Rintoul, S. R. The global influence of localized dynamics in the Southern Ocean. *Nature* **558**, 209–218 (2018).
- Sarmiento, J., Gruber, N., Brzezinski, M. & Dunne, J. High-latitude controls of thermocline nutrients and low latitude biological productivity. *Nature* **427**, 53–56 (2004).
- Brovkin, V., Ganopolski, A., Archer, D. & Rahmstorf, S. Lowering of glacial atmospheric CO₂ in response to changes in oceanic circulation and marine biogeochemistry. *Paleoceanography* **22**, PA4202 (2007).
- Hain, M. P., Sigman, D. M. & Haug, G. H. Carbon dioxide effects of Antarctic stratification, North Atlantic Intermediate Water

- formation, and subantarctic nutrient drawdown during the last ice age: diagnosis and synthesis in a geochemical box model. *Glob. Biogeochem. Cycles* **24**, GB4023 (2010).
10. Jaccard, S. L. et al. Two modes of change in southern ocean productivity over the past million years. *Science* **339**, 1419–1423 (2013).
 11. Martínez-García, A. et al. Iron fertilization of the Subantarctic Ocean during the last ice age. *Science* **343**, 1347–1350 (2014).
 12. Takahashi, T. Global sea-air CO₂ flux based on climatological surface ocean pCO₂, and seasonal biological and temperature effects. *Deep Sea Res. Part II* **49**, 1601–1622 (2002).
 13. Takahashi, T. et al. Climatological mean and decadal change in surface ocean pCO₂, and net sea–air CO₂ flux over the global oceans. *Deep Sea Res. Part II* **56**, 554–577 (2009).
 14. Volk, T. & Hoffert, M. I. *The Carbon Cycle and Atmospheric CO₂: Natural Variations Archaean to Present* Vol. 32, 99–110 (the American Geophysical Union, 1985).
 15. Hain, M., Sigman, D. & Haug, G. in *Treatise on Geochemistry* 2nd ed., Vol. 8, 485–517 (Elsevier, 2014).
 16. Takahashi, T., Olafsson, J., Goddard, J. G., Chipman, D. W. & Sutherland, S. C. Seasonal variation of CO₂ and nutrients in the high-latitude surface oceans: a comparative study. *Glob. Biogeochem. Cycles* **7**, 843–878 (1993).
 17. Khatiwala, S., Schmittner, A. & Muglia, J. Air–sea disequilibrium enhances ocean carbon storage during glacial periods. *Sci. Adv.* **5**, eaaw4981 (2019).
 18. Köhler, P., Fischer, H., Munhoven, G. & Zeebe, R. E. Quantitative interpretation of atmospheric carbon records over the last glacial termination. *Glob. Biogeochem. Cycles* **19**, GB4020 (2005).
 19. Heinze, C., Maier-Reimer, E. & Winn, K. Glacial pCO₂ reduction by the world ocean: experiments with the Hamburg carbon cycle model. *Paleoceanography* **6**, 395–430 (1991).
 20. Sarmiento, J. L. & Gruber, N. *Ocean Biogeochemical Dynamics* (Princeton University Press, 2006).
 21. Wang, X. T. et al. Deep-sea coral evidence for lower Southern Ocean surface nitrate concentrations during the last ice age. *Proc. Natl Acad. Sci. USA* **114**, 3352–3357 (2017).
 22. Martínez-Boti, M. A. et al. Boron isotope evidence for oceanic carbon dioxide leakage during the last deglaciation. *Nature* **518**, 219–222 (2015).
 23. Shuttleworth, R. et al. Early deglacial CO₂ release from the Sub-Antarctic Atlantic and Pacific oceans. *Earth Planet. Sci. Lett.* **554**, 116649 (2021).
 24. Martínez-García, A. et al. Southern Ocean dust–climate coupling over the past four million years. *Nature* **476**, 312–315 (2011).
 25. Pedro, J. B. et al. The spatial extent and dynamics of the Antarctic Cold Reversal. *Nat. Geosci.* **9**, 51–55 (2015).
 26. Jouzel, J. et al. Orbital and millennial Antarctic climate variability over the past 800,000 years. *Science* **317**, 793–796 (2007).
 27. Benz, V., Esper, O., Gersonde, R., Lamy, F. & Tiedemann, R. Last Glacial Maximum sea surface temperature and sea-ice extent in the Pacific sector of the Southern Ocean. *Quat. Sci. Rev.* **146**, 216–237 (2016).
 28. Menviel, L. et al. Southern Hemisphere westerlies as a driver of the early deglacial atmospheric CO₂ rise. *Nat. Commun.* **9**, 2503 (2018).
 29. Gregor, L. & Gruber, N. OceanSODA-ETHZ: a global gridded data set of the surface ocean carbonate system for seasonal to decadal studies of ocean acidification. *Earth Syst. Sci. Data* **13**, 777–808 (2021).
 30. Raitzsch, M. et al. Boron isotope-based seasonal paleo-pH reconstruction for the Southeast Atlantic – a multispecies approach using habitat preference of planktonic foraminifera. *Earth Planet. Sci. Lett.* **487**, 138–150 (2018).
 31. Foster, G. L. Seawater pH, pCO₂ and [CO₃²⁻] variations in the Caribbean Sea over the last 130 kyr: A boron isotope and B/Ca study of planktic foraminifera. *Earth Planet. Sci. Lett.* **271**, 254–266 (2008).
 32. Bostock, H. C., Hayward, B. W., Neil, H. L., Sabaa, A. T. & Scott, G. H. Changes in the position of the Subtropical Front south of New Zealand since the last glacial period. *Paleoceanography* **30**, 824–844 (2015).
 33. Sikes, E. L. et al. Southern Ocean seasonal temperature and Sub-tropical Front movement on the South Tasman Rise in the late Quaternary. *Paleoceanography* **24**, PA2201 (2009).
 34. Belkin, I. M. & Gordon, A. L. Southern Ocean fronts from the Greenwich meridian to Tasmania. *J. Geophys. Res. Oceans* **101**, 3675–3696 (1996).
 35. Elderfield, H. & Ganssen, G. Past temperature and δ¹⁸O of surface ocean waters inferred from foraminiferal Mg/Ca ratios. *Nature* **405**, 442–445 (2000).
 36. Dai, Y., Yu, J. & Rafter, P. A. Deglacial ventilation changes in the deep Southwest Pacific. *Paleoceanogr. Paleoclimatol* **36**, e2020PA004172 (2021).
 37. Ren, H. et al. Glacial-to-interglacial changes in nitrate supply and consumption in the subarctic North Pacific from microfossil-bound N isotopes at two trophic levels. *Paleoceanography* **30**, 1217–1232 (2015).
 38. Ren, H., Sigman, D. M., Thunell, R. C. & Prokopenko, M. G. Nitrogen isotopic composition of planktonic foraminifera from the modern ocean and recent sediments. *Limnol. Oceanogr.* **57**, 1011–1024 (2012).
 39. Studer, A. S. et al. Increased nutrient supply to the Southern Ocean during the Holocene and its implications for the pre-industrial atmospheric CO₂ rise. *Nat. Geosci.* **11**, 756–760 (2018).
 40. Studer, A. S. et al. Antarctic Zone nutrient conditions during the last two glacial cycles. *Paleoceanography* **30**, 845–862 (2015).
 41. Ai, X. E. et al. Southern Ocean upwelling, Earth’s obliquity, and glacial-interglacial atmospheric CO₂ change. *Science* **370**, 1348–1352 (2020).
 42. Li, T. et al. Rapid shifts in circulation and biogeochemistry of the Southern Ocean during deglacial carbon cycle events. *Sci. Adv.* **6**, eabb3807 (2020).
 43. Monnin, E. et al. Evidence for substantial accumulation rate variability in Antarctica during the Holocene, through synchronization of CO₂ in the Taylor Dome, Dome C and DML ice cores. *Earth Planet. Sci. Lett.* **224**, 45–54 (2004).
 44. Marcott, S. A. et al. Centennial-scale changes in the global carbon cycle during the last deglaciation. *Nature* **514**, 616–619 (2014).
 45. Lambert, F. et al. Dust–climate couplings over the past 800,000 years from the EPICA Dome C ice core. *Nature* **452**, 616–619 (2008).
 46. Sachs, J. P. & Anderson, R. F. Fidelity of alkenone paleotemperatures in southern Cape Basin sediment drifts. *Paleoceanography* **18**, 1082 (2003).
 47. Anderson, R. F. et al. Biological response to millennial variability of dust and nutrient supply in the Subantarctic South Atlantic Ocean. *Philos. Trans. A Math. Phys. Eng. Sci.* **372**, 20130054 (2014).
 48. Garcia, H. E. et al. World Ocean Atlas 2018. Vol. 4: dissolved inorganic nutrients (phosphate, nitrate and nitrate+nitrite, silicate). A. Mishonov Technical Editor, NOAA Atlas NESDIS 84, 35pp. https://www.ncei.noaa.gov/sites/default/files/2020-04/woa18_vol4.pdf (2019).
 49. Locarnini, R. A. et al. World Ocean Atlas 2018, Volume 1: Temperature. A. Mishonov, Technical Editor. NOAA Atlas NESDIS 81, 52pp. https://www.ncei.noaa.gov/sites/default/files/2020-04/woa18_vol1.pdf (2019).
 50. Barker, S., Greaves, M. & Elderfield, H. A study of cleaning procedures used for foraminiferal Mg/Ca paleothermometry. *Geochem. Geophys. Geosyst.* **4**, 8407 (2003).
 51. Boyle, E. & Keigwin, L. Comparison of Atlantic and Pacific paleochemical records for the last 215,000 years: Changes in deep ocean circulation and chemical inventories. *Earth Planet. Sci. Lett.* **76**, 135–150 (1985).

52. Yu, J., Elderfield, H., Greaves, M. & Day, J. Preferential dissolution of benthic foraminiferal calcite during laboratory reductive cleaning. *Geochem. Geophys. Geosyst.* **8**, Q06016 (2007).
 53. Yu, J., Day, J., Greaves, M. & Elderfield, H. Determination of multiple element/calcium ratios in foraminiferal calcite by quadrupole ICP-MS. *Geochem. Geophys. Geosyst.* **6**, Q08P01 (2005).
 54. Farmer, J. R., Hönisch, B. & Uchikawa, J. Single laboratory comparison of MC-ICP-MS and N-TIMS boron isotope analyses in marine carbonates. *Chem. Geol.* **447**, 173–182 (2016).
 55. Shao, J. et al. Atmosphere-ocean CO₂ exchange across the last deglaciation from the boron isotope proxy. *Paleoceanogr. Paleoclimatol.* **34**, 1650–1670 (2019).
 56. Moy, A. D. et al. Varied contribution of the Southern Ocean to deglacial atmospheric CO₂ rise. *Nat. Geosci.* **12**, 1006–1011 (2019).
 57. Lewis, E., Wallace, D. & Allison, L. J. *Program Developed for CO₂ System Calculations* (Carbon Dioxide Information Analysis Center, managed by Lockheed Martin Energy Research Corporation for the US Department of Energy Tennessee, 1998).
 58. Lougheed, B. C. & Obrochta, S. P. A rapid, deterministic age-depth modeling routine for geological sequences with inherent depth uncertainty. *Paleoceanogr. Paleoclimatol.* **34**, 122–133 (2019).
 59. Yu, J. et al. More efficient North Atlantic carbon pump during the Last Glacial Maximum. *Nat. Commun.* **10**, 2170 (2019).
 60. Ren, H. et al. Impact of glacial/interglacial sea level change on the ocean nitrogen cycle. *Proc. Natl Acad. Sci. USA* **114**, E6759–E6766 (2017).
 61. Braman, R. S. & Hendrix, S. A. Nanogram nitrite and nitrate determination in environmental and biological materials by vanadium (III) reduction with chemiluminescence detection. *Anal. Chem.* **61**, 2715–2718 (1989).
 62. Weigand, M. A., Foriel, J., Barnett, B., Oleynik, S. & Sigman, D. M. Updates to instrumentation and protocols for isotopic analysis of nitrate by the denitrifier method. *Rapid Commun. Mass Spectrom.* **30**, 1365–1383 (2016).
- measurements. J.Y. supervised geochemical measurements made by Y.D. and X.J. H.R. made nitrogen isotope measurements. Y.D. performed data analyses and visualization. Y.D. wrote the first draft of the manuscript with significant inputs from J.Y. All authors contributed to the interpretation of the data and refinement of the manuscript.

Funding

Open access funding provided by Lund University.

Competing interests

The authors declare no competing interests.

Additional information

Supplementary information The online version contains supplementary material available at <https://doi.org/10.1038/s41467-022-32895-9>.

Correspondence and requests for materials should be addressed to Yuhao Dai or Jimin Yu.

Peer review information *Nature Communications* thanks Amy King for her contribution to the peer review of this work. Peer reviewer reports are available.

Reprints and permission information is available at <http://www.nature.com/reprints>

Publisher's note Springer Nature remains neutral with regard to jurisdictional claims in published maps and institutional affiliations.

Open Access This article is licensed under a Creative Commons Attribution 4.0 International License, which permits use, sharing, adaptation, distribution and reproduction in any medium or format, as long as you give appropriate credit to the original author(s) and the source, provide a link to the Creative Commons license, and indicate if changes were made. The images or other third party material in this article are included in the article's Creative Commons license, unless indicated otherwise in a credit line to the material. If material is not included in the article's Creative Commons license and your intended use is not permitted by statutory regulation or exceeds the permitted use, you will need to obtain permission directly from the copyright holder. To view a copy of this license, visit <http://creativecommons.org/licenses/by/4.0/>.

© The Author(s) 2022

Acknowledgements

We thank Brad Opdyke and Will Howard for help with arranging core materials, and Laurie Menviel for providing model outputs. This work is supported by NSFC42076056 and ARC Discovery Project DP190100894 to J.Y., and Ministry of Science and Technology, Taiwan (111-2636-M-002-020) to H.R.

Author contributions

J.Y. designed the project. Y.D. derived the pCO₂ decomposition method. Y.D. made boron isotope measurements. X.J. made new trace element